Red emission enhancement in $BaYF_5$:Eu^{3+} phosphor nanoparticles by Bi^{3+} co-doping

KATARINA MILENKOVIĆ,[1] LJUBICA ĐAČANIN FAR,[1] SANJA KUZMAN,[1] ŽELJKA ANTIĆ,[1] ALEKSANDAR ĆIRIĆ,[1] (iD) MIROSLAV D. DRAMIĆANIN,[1,2] AND BOJANA MILIĆEVIĆ[1,3]

[1] *Centre of Excellence for Photoconversion, Vinča Institute of Nuclear Sciences—National Institute of the Republic of Serbia, University of Belgrade, 11001 Belgrade, Serbia*
[2] *bojanam@vinca.rs*
[3] *dramican@vinca.rs*

Abstract: Herein, we report the photoluminescence properties of Bi^{3+}-sensitized BaYF5: 10 mol%Eu^{3+} nanoparticles. The emission spectra feature Eu^{3+} peaks corresponding to transitions from the $^5D0$ excited to ^7FJ (J = 1, 2, 3, 4) lower levels with two dominant emissions positioned in the orange-red ($\sim$ 592 nm, $^5D0 \rightarrow {}^7F1$) and deep-red ($\sim$ 697 nm, $^5D0 \rightarrow {}^7F4$) regions. Upon 265 nm excitation, the emission intensity increases with an increase of Bi^{3+} concentration up to 20 mol%. Due to the energy transfer from Bi^{3+} to Eu^{3+} ions, the integrated intensity of Eu^{3+} emission in the Bi^{3+} co-doped BaYF5:10 mol%Eu^{3+} is 216% stronger than in the Bi^{3+}-free sample. Our findings demonstrated that BaYF5:Eu,Bi has potential in plant lighting technology due to strong emission in red and deep-red spectral areas.

1. Introduction

Nanometric luminescent materials, especially those doped with lanthanide ions, are getting a lot of attention because they can be used in many different areas. They can be used in light-emitting devices, optical amplifiers, near-infrared photodetectors, biological labeling, clinical diagnostics, medical imaging, anti-counterfeiting, latent fingerprint detection, and more [1–9]. Among them, nanometric metal fluorides such as alkali-metal lanthanide fluorides or alkaline-earth-metal lanthanide fluorides offer various advantages, including low phonon energy, electron-acceptor behavior, wide optical transmission domain, high resistivity, and anionic conductivity. Cubic BaF_2 and CaF_2 exhibit high optical transparency within the 0.14–13 µm and 0.12–10 µm wavelength ranges, respectively [10]. The wide band gap (> 9 eV) of these fluoride materials ensures allowed electronic transitions of the dopant ions while preventing self-absorption [10]. In addition, fluoride materials have a low phonon frequency (300–500 cm^{-1}), which reduces non-radiative relaxation while increasing emission efficiency [11]. For example, LaF_3 and CaF_2 have effective phonon energies of 43.4 meV (350 cm^{-1}) and 40.7 meV (328 cm^{-1}), respectively [12,13].

Ba^{2+}-containing lanthanide fluorides, an important subset of the lanthanide fluoride family, have been recognized as promising host materials for upconversion luminescence. Many studies have found that Yb^{3+}/Ho^{3+}, Yb^{3+}/Er^{3+}, or Yb^{3+}/Tm^{3+} activated $BaYF_5$, $BaGdF_5$, or $BaLuF_5$ hosts can boost emissions from lower-energy states, which is valuable for bioimaging applications [14–22]. Furthermore, Qiu *et al.* demonstrate that these nanophosphors with considerable near infrared-to-visible multicolor upconversion emissions can be soluble in organic solvents and water *via* a surface poly(acrylic acid) ligand exchange reaction [20]. Pr^{3+}-doped $BaYF_5$ nanoparticles showed remarkable UVC emission when exposed to either UV or blue-light excitations, suggesting that have significant potential in various UV-requiring applications, such as security industries, phototherapy, and sterilization [23]. On the other hand, the literature reports on the Eu^{3+}-doped luminescence in $BaYF_5$ nanophosphors are scarce [24].

Eu^{3+} with the $4f^6$ electronic configuration was discovered to be the most efficient lanthanide red-emitting ion. Eu^{3+} exhibits multi-color emissions, including orange, red, and deep red, corresponding to transitions from the $^5D_0$ excited emitting level to ^7F_J ($J = 1, 2, 3,$ and 4) lower levels [25]. Eu^{3+} doped fluoride materials are typically activated *via* F^- − Eu^{3+} charge transfer or directly exciting $4f^n$ energy levels. However, Eu^{3+}-activated phosphors exhibit poor absorption in the UV or blue spectrum due to the parity-forbidden $4f \rightarrow 4f$ transitions. This limits their usage in practical applications. Co-doping with another lanthanide or transition metal ions is an effective strategy to overcome this obstacle. This strategy broadens the excitation spectrum and increases luminescence intensity by transferring energy from the sensitizer to the activator ion [26]. Research on Eu^{3+} sensitization is ongoing, as the quest for narrow-band red-emitting phosphors that can be used in phosphor-converted LEDs has not yet reached its highest point.

Blasse showed that energy transfer between Ce^{3+} and Eu^{3+} is inefficient due to metal-to-metal charge transfer quenching ($Ce^{3+}/Eu^{3+} \rightarrow Ce^{4+}/Eu^{2+}$) [27,28]. The quantum efficiency of Ce^{3+} excitation in $YF_3:Ce^{3+}$, Eu^{3+} was reduced to approximately 1%. However, efficient sensitization of Eu^{3+} emission can be achieved by inhibiting metal-to-metal charge transfer through spatial separation of sensitizer ions and Eu^{3+} [29]. Aside from Ce^{3+}, Bi^{3+} can also act as a sensitizer to widen the Eu^{3+} absorption spectrum response, enhancing the luminescent intensity of Eu^{3+}. For example, Luo *et al.* found that Bi^{3+}-doped $BaYF_5:Yb^{3+}$, Er^{3+} phosphors have 3–4 times stronger upconversion luminescence than a Bi^{3+}-free sample [18]. Mancebo *et al.* found that the luminescence of co-doped $LaF_3:Eu^{3+}$, Bi^{3+}, through the $Bi^{3+} \rightarrow Eu^{3+}$ energy-transfer band, enhancing the emission intensity by more than one order of magnitude, because the presence of bismuth in the nanoparticles composition increases the material's X-ray attenuation capacity [30].

Herein, we explore the sensitization of Eu^{3+} emission with Bi^{3+} in $BaYF_5:Eu^{3+}$, Bi^{3+} (BYF: Eu, Bi) phosphor nanoparticles and gain insight into the relevant energy transfer mechanism. A set of samples with an average particle size of about 33 nm was synthesized using a solvothermal method. The concentration-dependent luminescence properties reveal that the luminescence of a representative $BYF:10Eu^{3+},20Bi^{3+}$ phosphor is 216% enhanced *via* energy transfer from Bi^{3+} to Eu^{3+} upon the UV excitation. The most noticeable emission peaks are at 590 nm (orange-red) and 700 nm (deep-red), with the latter being more pronounced. Moreover, the energy transfer efficiency (η_T), Eu^{3+}-Bi^{3+} critical distance (R_c), and energy transfer mechanism from Bi^{3+} to Eu^{3+} ions in BYF: Eu^{3+}, Bi^{3+} nanophosphors were discussed. Our findings indicate that BYF: Eu^{3+} phosphor nanoparticles with a unique feature of intense emission at around 700 nm could be used in various applications, particularly sustainable agriculture.

2. Experimental section

2.1. Materials

Yttrium(III) nitrate hexahydrate ($Y(NO_3)_3 \cdot 6H_2O$, 99.8%) was purchased from Aldrich, while bismuth(III) nitrate pentahydrate ($Bi(NO_3)_3 \cdot 5H_2O$, 98.0%) was from Reanal. Europium(III) nitrate hexahydrate ($Eu(NO_3)_3 \cdot 6H_2O$, 99.9%), barium nitrate ($Ba(NO_3)_2$, 99.95%) and ammonium fluoride (NH_4F, 98%) were obtained from Alfa Aesar. Glycerol ($\geq 99\%$) was purchased from Acros Organics. All the materials were used without further purification.

2.2. Synthesis of $BaYF_5$: Eu, Bi

We synthesized three sets of nanophosphors using the solvothermal method: 1. $BaYF_5$: xEu, where $x = 1, 10, 20$ mol%; 2. $BaYF_5$: 10Eu, yBi, where $y = 0, 5, 10, 20, 30, 50$ mol%; and 3. $BaYF_5$: xEu, 20Bi where $x = 1, 5, 10, 20$ mol%. From the first set, we chose the sample with 10 mol% of Eu^{3+} as a representative for further co-doping with Bi^{3+} (samples of set No. 2) as it

had the most intense emission (see Fig. S1). The third sample set was prepared to gain insight into energy transfer mechanisms.

Each synthesis was conducted through the steps presented in Fig. 1. Initially, $Ba(NO_3)_2$, Ln-nitrates, and $Bi(NO_3)_3$ were weighted according to the stoichiometric ratio (nominal amounts in precursor mixture are presented in Table 1) and dissolved in 7.0 ml water and 7.5 ml glycerol. After that, an excess amount of NH_4F was dissolved in 1.0 ml water and added dropwise to the initial solution. The resulting solution was maintained with a strong stirring for 1 h at room temperature. This mixture was then transferred into a 50-mL Teflon-lined autoclave and heated in the oven at 180°C for 21 h. The obtained nanoparticles were centrifuged at 4000 rpm for 10 minutes, washed in water and ethanol:water = 1:1 mixture, and air dried before further characterization.
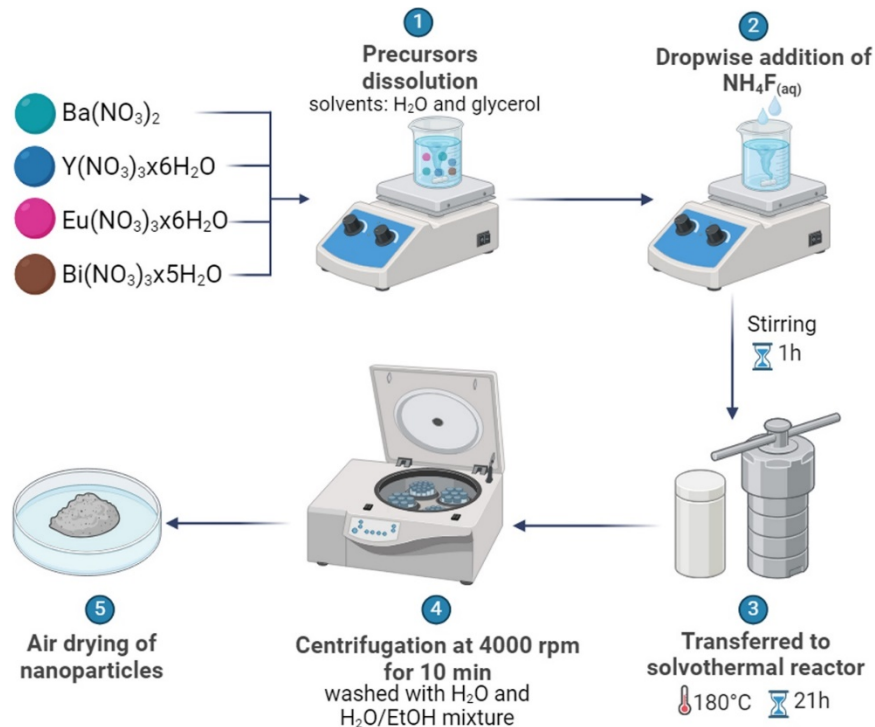
Fig. 1. Schematic illustration of the solvothermal synthesis of BYF: Eu, Bi nanoparticles. The precursors were initially dissolved in a water-glycerol mixture and fluoride ions were added dropwise (steps 1 and 2). After vigorous stirring, the resulting mixture was transferred to a Teflon-lined autoclave and heated to 180°C for 21 h (step 3). The resulting nanoparticles were subsequently washed, centrifuged, and left to dry in air (steps 4 and 5).

2.3. Instruments and measurements

Powder X-ray diffraction (PXRD) measurements were performed on a Rigaku SmartLab system (Tokyo, Japan) operating with Cu Kα radiation (30 mA, 40 kV). Diffraction data sets were recorded with a step size of 0.02° and a counting time of 1°/min in 2θ range from 10° to 90°. Results of the structural analysis (unit cell parameters, microstrain values, and data fit parameters) were obtained using the built-in PDXL2 software. The average particle size was calculated using ImageJ software. Shimadzu UV-2600 (Shimadzu Corporation, Tokyo, Japan) spectrophotometer with an integrating sphere was used to measure diffuse reflectance spectra with

Table 1. The final precursor quantities for synthesis of the representative BYF:10Eu, yBi (y = 0, 5, 10, 20, 30, 50 mol%) sample set

Bi^{3+} (mol%)	$Ba(NO_3)_2$ (mmol)	$Y(NO_3)_3 \cdot 6H_2O$ (mmol)	$Eu(NO_3)_3 \cdot 6H_2O$ (mmol)	$Bi(NO_3)_3$ (mmol)	NH_4F (mmol)
0		0.90		/	
5		0.85		0.05	
10	1.00	0.80	0.10	0.10	7.00
20		0.70		0.20	
30		0.60		0.30	
50		0.40		0.50	

$BaSO_4$ as a reference. The photoluminescent emission and excitation spectra were acquired using a Fluorolog-3 Model FL3-221 spectrofluorometer system (Horiba-Jobin-Yvon) under continuous operation with a 450W xenon lamp. The field emission scanning electron microscope TESCAN MIRA3 was used to observe the microstructure and particle size of the examined nanopowders.
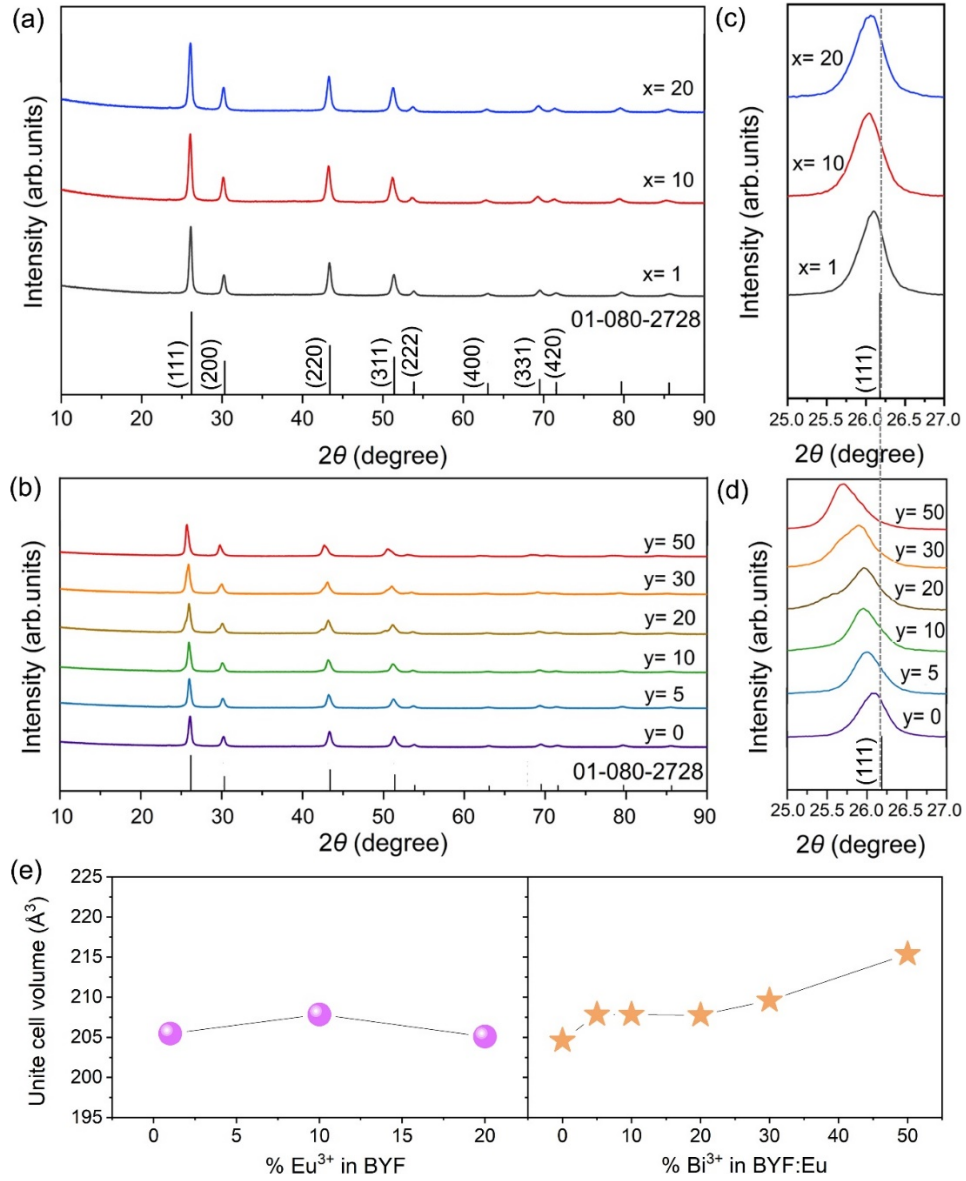
3. Results and discussion

3.1. PXRD and morphology analysis

Despite the addition of Eu^{3+} and Bi^{3+} ions, the main diffraction peaks of BYF: xEu, $x = 1-20$ mol% (Fig. 2(a)) and BYF:10Eu, $y$$Bi^{3+}$, $y = 0-50$ mol% nanophosphors (Fig. 2(b)), correspond to the main reflections from 111, 200, 220, 311, 222, 400, 331, 420, 422, and 511 crystal planes and resemble standard cubic data of ICDD No. 01-080-2728 for single-phase $BaYF_5$, space group $Fm\bar{3}m$ (225). Compared to the standard cubic $BaYF_5$, the magnified (111) diffraction peaks of BYF: Eu samples are slightly shifted to the lower 2θ values due to the replacement of Y^{3+} (r = 0.9 Å, ionic radii, VI coordinated) by a larger Eu^{3+} (r = 0.947 Å, ionic radii, VI coordinated) as shown in Fig. 2(c) [31]. The magnified (111) diffraction peaks of BYF: 10Eu, yBi samples are shifted more to the lower 2θ values due to the replacement of Y^{3+} by two larger Eu^{3+} and Bi^{3+} ions (r = 1.03 Å, ionic radii, VI coordinated) as shown in Fig. 2(d) [31]. Also, the degree of deviation in the shape of these diffraction peaks increases when the Bi^{3+} concentration exceeds 20 mol%, suggesting that high Bi^{3+} concentrations affect the crystal structure of the cubic $BaYF_5$ host lattice. Nonetheless, these results indicate that doping with a small amount of Bi^{3+} does not strongly affect the phase structure of $BaYF_5$ while higher doping concentrations distort $BaYF_5$ host lattice that, however, still resembles cubic. Figure 2(e) (left) shows that as the Eu^{3+} content increases, the unit cell volume in BYF fluctuates slightly. Figure 2(e) (right) shows a considerable increase in the unit cell volume of the BYF:10Eu, yBi system as the Bi^{3+} concentration increases due to a larger distinction in Bi^{3+} and Y^{3+} ionic radius.

Table 2 shows the results of the structural analysis: crystallite size (CS), microstrain values, unit cell parameters, unit cell volume (CV), and data fit parameters (R_{wp}, R_p, R_e, GOF) of BYF:10Eu, yBi ($y = 0$, 5, 10, 20, 30, and 50 mol%) nanophosphors. The CS of BYF:10Eu is estimated to be 19.6 nm, and the lattice constant a is 5.8925 Å (CV = 204.60 Å^3). The influence of Bi^{3+} doping in the BYF: 10Eu lattice causes crystal lattice expansion up to $a = 5.9942$ Å, CV = 215.37 Å^3 for the sample BYF:10Eu, 50Bi. As previously stated, expansion is expected when dopants with a larger ionic radius replace the Y^{3+} with a smaller ionic radius in $BaYF_5$.

Figure 3 shows SEM images of BYF:10Eu phosphor nanoparticles with a particle size distribution. Nanoparticles are of a quasispherical shape, as well as a high degree of crystallinity. The average crystalline size of BYF: 10Eu nanoparticles, considering more than 100 particles, was estimated to be 33 ± 2 nm (see Fig. 3(c)). The average particle size was calculated without considering partially displayed particles. The histogram was fitted using a lognormal distribution.

Fig. 2. PXRD patterns of (a) BYF: xEu ($x = 1$, 10, and 20 mol%) and (b) BYF:10Eu, yBi ($y = 0$, 5, 10, 20, 30, and 50 mol%) nanoparticles; (c) The evolution of the (111) diffraction peak magnified from (a); (d) The evolution of the (111) diffraction peak magnified from (b); (e) The values of the unit cell volume versus Eu^{3+} and Bi^{3+} contents in BYF (purple circles) and BYF: 10Eu (orange stars), respectively.
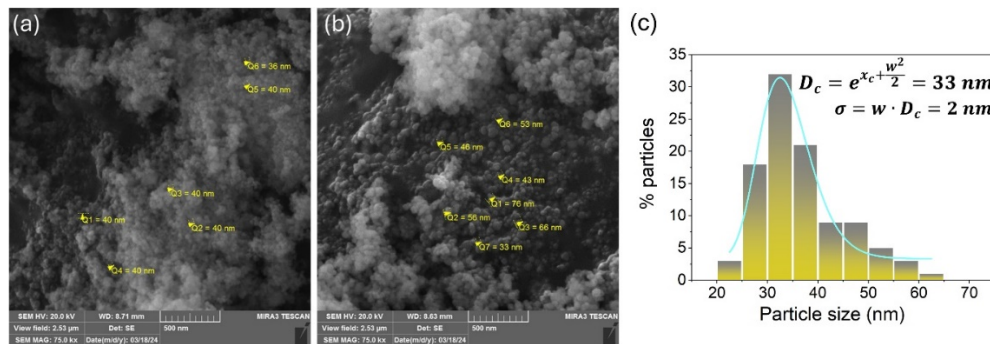
Table 2. Results of the structural analysis of BYF: 10Eu, *y*Bi nanophosphors, where *y* = 0, 5, 10, 20, 30, and 50 mol% Bi³⁺

Bi³⁺ content (mol%)	0	5	10	20	30	50
a = b = c (Å)	5.8925 (3)	5.9236 (4)	5.9235 (5)	5.9227 (6)	5.9401 (6)	5.9942 (5)
CV (Å³)	204.60 (4)	207.85 (5)	207.84 (6)	207.76 (7)	209.60 (7)	215.37 (6)
CS (Å)	196 (3)	274 (5)	305 (12)	198 (11)	100 (6)	95 (5)
Strain	0.46 (3)	0.64 (2)	0.75 (2)	1.03 (6)	0.23 (3)	0.26 (3)
GOF	1.1254	1.5272	1.6212	1.6678	2.9693	3.6494
[a]R$_{wp}$	4.23	5.79	6.14	6.42	11.08	13.43
[b]R$_p$	3.16	4.45	4.66	4.95	7.57	8.71
[c]R$_e$	3.75	3.79	3.78	3.85	3.73	3.68

[a]R$_{wp}$—the weighted profile factor;
[b]R$_p$—the profile factor;
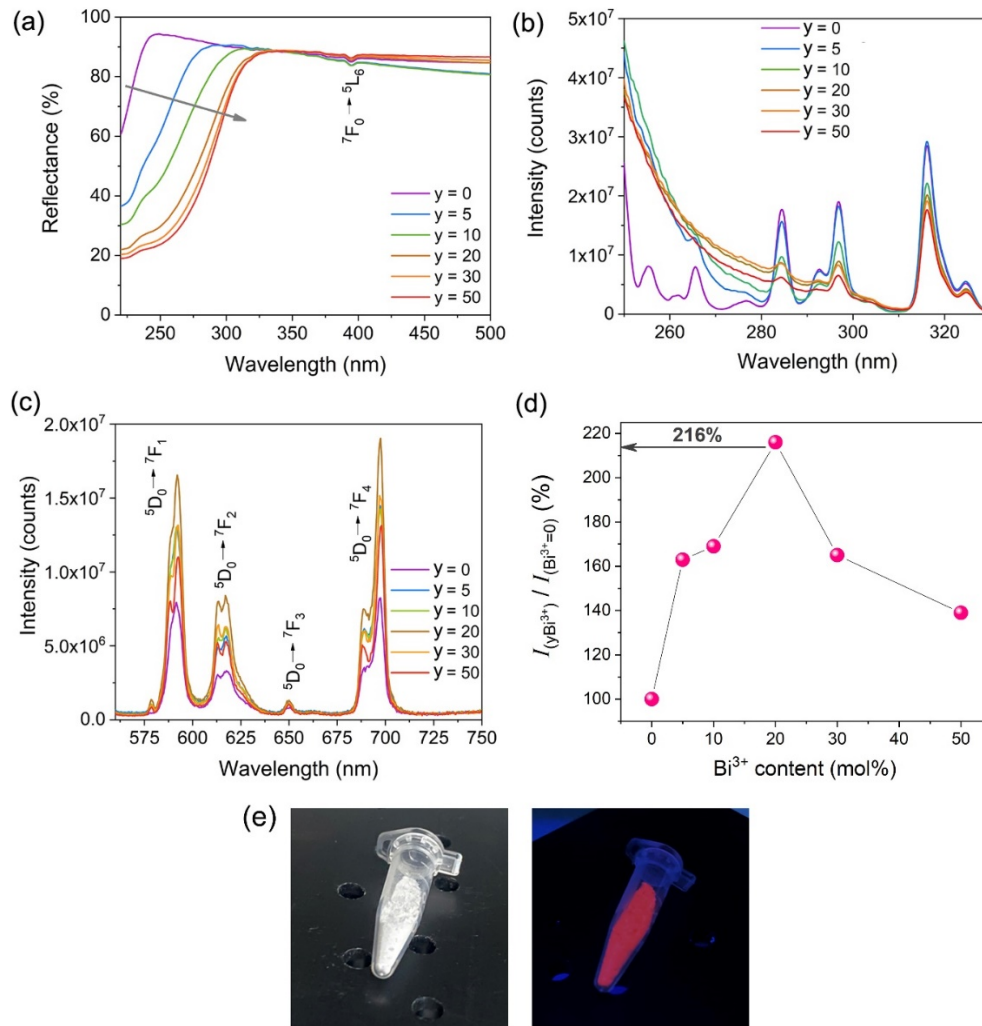[c]R$_e$—the expected weighted profile factor; GOF—the goodness of fit.

Fig. 3. (a, b) SEM images of solvothermally synthesized BYF: 10Eu phosphor nanoparticle; (c) The particle size distribution.

3.2. Spectroscopic properties

Figure 4(a) shows the room temperature diffuse reflectance spectra of BYF:10Eu, *y*Bi (*y* = 0, 5, 10, 20, 30, and 50 mol%) samples in the 220–500 nm wavelength range. The spectra reveal the absorption band of Eu³⁺ at 394 nm, originating from the ground state $^7F_0$ to the upper level $^5L_6$ transition. In addition, it is observed that the UV band edge tends to shift towards lower energy with an increase of Bi³⁺ content in the BYF: Eu. This red shift with the change of Bi³⁺ content indicates a strong absorption of Bi³⁺, which lies in the UV region [32–34]. The spectroscopic properties of a representative Bi³⁺ co-doped BYF: 10Eu phosphor are analyzed, whereas Fig. S1 shows the photoluminescence excitation and emission spectra of Bi-free BYF with varying Eu³⁺ contents (see Supplement 1). The room temperature photoluminescence excitation spectra of all BYF: Eu, Bi samples recorded in the 250–330 nm (λ_{em} = 698 nm) wavelength range are given in Fig. 4(b). The intense peaks at 297 and 317 nm correspond to the $^7F_0 \rightarrow {}^5F_J$ and $^7F_0 \rightarrow {}^5H_J$ transitions of Eu³⁺, respectively [35,36]. A red shift is also observed with increasing Bi³⁺ content. This suggests that Bi³⁺ may act as a sensitizer, broadening the Eu³⁺ absorption spectrum response and increasing the luminous intensity of Eu³⁺.

The photoluminescence emission spectra of all BYF: Eu, Bi samples recorded at room temperature are displayed in Fig. 4(c) (λ_{ex} = 265 nm). All emissions correspond to $4f$–$4f$ transitions of Eu³⁺ are located at ~594 nm ($^5D_0 \rightarrow {}^7F_1$), ~613 nm ($^5D_0 \rightarrow {}^7F_2$), ~650 nm ($^5D_0 \rightarrow {}^7F_3$), and ~700 nm ($^5D_0 \rightarrow {}^7F_4$). The emission in the deep-red spectral region around 700

Fig. 4. (a) Room temperature diffuse reflectance spectra for BYF: 10Eu, yBi ($y = 0$, 5, 10, 20, 30, and 50 mol%) samples; Room temperature photoluminescence for BYF: 10Eu, yBi ($y = 0$, 5, 10, 20, 30, and 50 mol%) samples: (b) Excitation spectra under $\lambda_{em} = 698$ nm; (c) Emission spectra under $\lambda_{ex} = 265$ nm; (d) Ratio of the integrated emission intensity for BYF: 10Eu samples with varied Bi concentration and Bi-free BYF: 10Eu sample as a function of Bi^{3+} ions concentration; (e) The appearance of representative BYF: 10Eu, 20Bi phosphor nanoparticles under daylight (left) and UV light (right).

nm, corresponding to the $^5D_0 \rightarrow {}^7F_4$ transition, exhibits the highest intensity in these spectra. This is not common for Eu^{3+}, but it has been reported for several hosts where the structural distortion from octahedral symmetry to non-centrosymmetric D_{4d} exists [37,38], as odd-rank components of the static forced electric dipole and ligand polarizability-dependent dynamic coupling mechanisms are high, particularly in the highly polarizable chemical environment [39]. Figure 4(d) shows that europium's photoluminescent intensity continually increases until the Bi^{3+} content reaches 20 mol%, while the further addition of Bi^{3+} decreases the emission intensity. The integrated emission intensity in the 520–720 nm wavelength range shows that the representative BYF: 10Eu, 20Bi sample has a 216% emission enhancement compared to the Bi-free BYF: 10Eu

phosphor. Figure 4(e) shows the translucent white color of representative BYF: 10Eu, 20Bi phosphor nanoparticles under daylight (left) and the red appearance under UV light (right).

3.3. Energy transfer in BYF: Bi Eu, phosphor nanoparticles

The third set of BYF samples with constant Bi^{3+} ($y = 20$ mol%) and various Eu^{3+} ($x = 1, 5, 10,$ 20 mol%) contents was prepared to examine the energy transfer mechanism from a sensitizer to an activator. Fig. S2 with the XRD spectra confirms the phase purity of these samples (see Supplement 1). Figure 5(a) and 5(b) show the photoluminescence spectra of BYF nanoparticles with constant 20 mol% Bi and different Eu ($x = 1, 5, 10,$ and 20 mol%) concentrations. The photoluminescent spectra of BYF: Bi, Eu phosphors revealed a broadband blue emission centered at approximately 430 nm attributed to the $^3P_1 \rightarrow {}^1S_0$ allowed Bi^{3+} transition. These Figs. also show that $Bi^{3+} \rightarrow Eu^{3+}$ energy transfer in the BYF:xEu, 20Bi ($x = 1, 5, 10,$ and 20 mol%) system has a different character, depending on Bi^{3+} content.

Energy transfer from a sensitizer to an activator can occur *via* radiative transfer, exchange interaction, or multipole-multipole interaction [40]. Dips in the sensitizer's emission spectra that correlate to the absorption spectrum of activated ions demonstrate the possibility of radiative energy transfer from the sensitizer to the activator [41]. As shown in Fig. 5(b), the emission spectra of BYF: 20Bi, 20Eu clearly show a dip that overlaps with the absorption of Eu^{3+}, indicating that the energy transfer has a radiative character. On the other hand, Fig. 5(a) reveals that 20mol% Bi^{3+} and Eu^{3+} concentrations less than or equal to 10 mol% contribute to a non-radiative character of energy transfer in BYF: Bi, Eu.

According to the Dexter and Schulman theory, concentration quenching in inorganic phosphors occurs when energy passes from one activator to another, often until the energy sink in the lattice is achieved [42]. Blasse reported that the average separation distance between the sensitizer and activator ions is equal to the critical distance R_c, which can be expressed as follows [43]:

$$R_c \approx 2\left(\frac{3V}{4\pi C_{Bi+Eu}N}\right)^{1/3}, \tag{1}$$
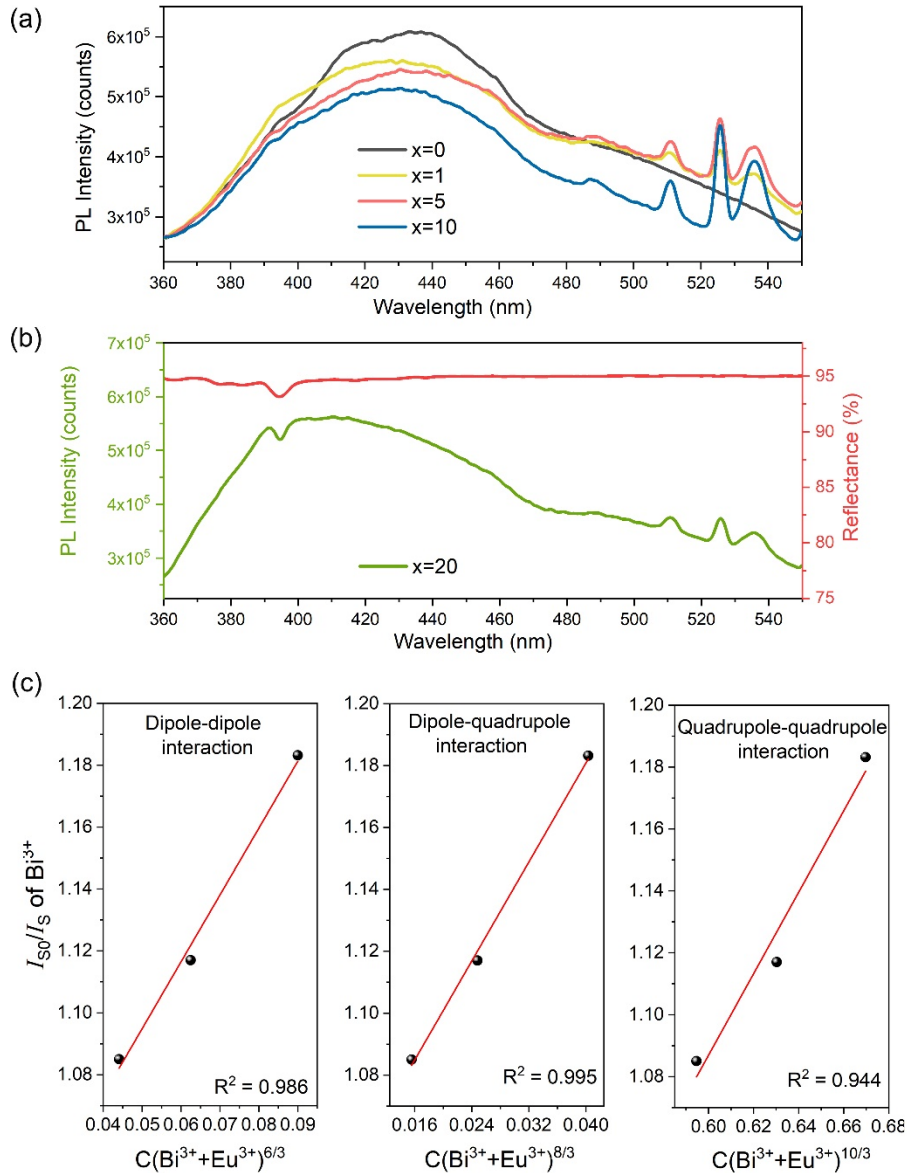
where N is the number of sites that lanthanide ions occupy per unit cell, V is the unit cell volume, and C_{Bi+Eu} is the overall doping concentration of the Bi^{3+} and Eu^{3+} ions. For $BaYF_5$, N = 2 and V = 204.34 Å^3. Using Eq. (1), R_c is determined to be 9.8, 9.2, and 8.7 Å for C_{Bi+Eu} = 0.21, 0.25, and 0.30, respectively. The critical concentration of C_{Bi+Eu} in the BYF host is 0.30, while higher concentrations show emission-quenching effects.

Non-radiative energy transfers include exchange interaction and multipole-multipole interaction. Exchange interaction occurs when the sensitizer and activator are separated by less than 5 Å and their orbitals overlap significantly [44]. In our case, the critical distance between Bi^{3+} and Eu^{3+} is 8.7 Å, excludes energy transfer *via* exchange interactions. Therefore, electric multipole-multipole interaction is a potential energy transfer mechanism in BYF: Bi, Eu nanophosphors when Bi^{3+} content is less than or equal to 10 mol%. Based on the Förster Resonance Energy Transfer formula of multipolar interaction and Reisfeld's approximation, the following relation can be given:

$$\frac{\eta_0}{\eta} \approx \frac{I_{S0}}{I_S} \propto C_{Bi+Eu}^{n/3}, \tag{2}$$

where η_0 and I_{S0} represent the emission quantum efficiency and luminescence intensity of the Bi^{3+} sensitizer ions alone, while η and I_S are the emission quantum efficiency and luminescence intensity of Bi^{3+} in the presence of Eu^{3+} activator ions. C_{Bi+Eu} is the overall doping concentration of the Bi^{3+} and Eu^{3+} ions, and $n = 6, 8,$ or 10 reflect dipole-dipole, dipole-quadrupole or quadrupole-quadrupole interactions, respectively. Equation (2) shows that the luminosity ratio I_{S0}/I_S can be used to estimate the amount of η_{S0}/η_S. Figure 5(c) depicts the linear plots between I_{S0}/I_S

Fig. 5. (a) The emission spectra of BYF: xEu, 20Bi ($x = 0$, 1, 5, and 10 mol%) nanoparticles; (b) Overlap of the emission spectrum of BYF: 20Eu, 20Bi and absorption of BYF: 10Eu; (c) Plots of I_{S0}/I_S versus C(Bi^{3+}+Eu^{3+})$^{6/3}$, C(Bi^{3+}+Eu^{3+})$^{8/3}$ and C(Bi^{3+}+Eu^{3+})$^{10/3}$.

and $C_{Bi+Eu}^{n/3}$ in all cases of electric multipole-multipole interaction. A good linear trend for n = 8 ($C_{Bi+Eu}^{8/3}$) shows that dipole-quadrupole interaction is the dominant mechanism for energy transfer from Bi^{3+} to Eu^{3+} in BYF phosphor nanoparticles.

The energy transfer efficiency (η_T) from a sensitizer to an activator ion can be calculated by the following relation [45,46]:

$$\eta_T = 1 - \frac{I_S}{I_{S0}} \tag{3}$$

Energy transfer efficiencies (η_T) of as-prepared samples increase with the increase of Eu^{3+} content with maximum values of 16% for representative BYF: 10Eu, 20Bi sample.

4. Conclusion

In this study, we synthesized three different sets of phosphor nanoparticles: $BaYF_5$: xEu, $BaYF_5$: 10Eu, yBi, and $BaYF_5$: xEu, 20Bi using the solvothermal method. All nanoparticles crystallize in a cubic structure, with the $Fm\bar{3}m$ (225) space group with an average particle size of around 33 nm. The diffuse reflectance spectra of the samples show a UV absorption band that shifts towards lower energy with the Bi^{3+} content increase. The excitation spectrum of $BaYF_5$: 10Eu exhibits typical transitions of Eu^{3+} and a red shift of a band tail as the Bi^{3+} content increases. The emission spectrum of $BaYF_5$: 10Eu, 20Bi with characteristic Eu^{3+} transition peaks in the red region shows a 216% enhanced intensity compared to Bi-free $BaYF_5$: 10Eu sample, while further addition of Bi^{3+} quenches the Eu^{3+} emission. These findings prove that Bi^{3+} is an excellent sensitizer ion for Eu^{3+} ion widening its absorption and enhancing its photoluminescent intensity. The Eu^{3+} major excitation band matches the Bi^{3+} emission band in the BYF: Bi, Eu system, indicating efficient energy transfer from Bi^{3+} to Eu^{3+}. The energy transfer mechanism for samples doped with up to $10\,mol\%$ Eu^{3+} is nonradiative due to dipole-quadrupole interactions. Higher doping concentration ($20\,mol\%$ Eu^{3+}) results in radiative energy transfer. The maximal energy transfer efficiency for BYF: 10Eu, 20Bi is 16%.

Disclosures. The authors declare no conflicts of interest.

Data availability. Data underlying the results presented in this paper are available upon reasonable request.

Supplemental document. See Supplement 1 for supporting content.

Reference

1. A. C. Berends, M. A. van de Haar, and M. R. Krames, "YAG:Ce^{3+} Phosphor: from micron-sized workhorse for general lighting to a bright future on the nanoscale," Chem. Rev. **120**(24), 13461–13479 (2020).
2. Y. Chen, J. Wei, J. Zhang, *et al.*, "Boosting the downconversion luminescence of Tm^{3+} -doped nanoparticles for s-band polymer waveguide amplifier," Nano Lett. **24**(4), 1399–1405 (2024).
3. L. Wang, R. Yan, Z. Huo, *et al.*, "Fluorescence resonant energy transfer biosensor based on upconversion-luminescent nanoparticles," Angew. Chem., Int. Ed. **44**(37), 6054–6057 (2005).
4. M.D. Dramićanin, *Luminescence Thermometry*, 1st ed., Elsevier, Woodhead publishing, 2018.
5. H. Li, G. Bai, Y. Lian, *et al.*, "Advances in near-infrared-activated lanthanide-doped optical nanomaterials: imaging, sensing, and therapy," Mater. Des. **231**, 112036 (2023).
6. L. Yan, L. Tao, Q. Zhang, *et al.*, "Amplifying photon upconversion in alloyed nanoparticles for a near-infrared photodetector," Nano Lett. **24**(15), 4580–4587 (2024).
7. E. Prabakaran and K. Pillay, "Nanomaterials for latent fingerprint detection: a review," J. Mater. Res. Technol. **12**, 1856–1885 (2021).
8. H. Suo, Q. Zhu, X. Zhang, *et al.*, "High-security anti-counterfeiting through upconversion luminescence," Mater. Today Phys. **21**, 100520 (2021).
9. Y. Fan, P. Wang, Y. Lu, *et al.*, "Lifetime-engineered NIR-II nanoparticles unlock multiplexed in vivo imaging," Nat. Nanotechnol. **13**(10), 941–946 (2018).
10. M.J. Weber, *CRC Handbook of laser Science and technology*, Volume 3, Optical Materials: Part 1, CRC press, Boca Ration, USA, 1986.
11. K.R.P. Alain Tressaud, eds., *Photonic and Electronic Properties of Fluoride Materials*, 1st Editio, Elsevier, 2016.
12. L. G. Jacobsohn, A. Toncelli, K. B. Sprinkle, *et al.*, "Spectral engineering of LaF_3:Ce^{3+} nanoparticles: The role of Ce^{3+} in surface sites," J. Appl. Phys. (Melville, NY, U. S.) **111**(7), 074315 (2012).
13. L. Su, J. Xu, Y. Xue, *et al.*, "Low-threshold diode-pumped Yb3+,Na+:CaF2 self-Q-switched laser," Opt. Express **13**(15), 5635 (2005).

14. F. Vetrone, V. Mahalingam, and J. A. Capobianco, "Near-infrared-to-blue upconversion in colloidal $BaYF_5$:Tm^{3+},Yb^{3+} nanocrystals," Chem. Mater. **21**(9), 1847–1851 (2009).

15. C. Zhang, P. An Ma, C. Li, *et al.*, "Controllable and white upconversion luminescence in BaYF5:Ln3+ (Ln = Yb, Er, Tm) nanocrystals," J. Mater. Chem. **21**(3), 717–723 (2011).

16. H. Liu, W. Lu, H. Wang, *et al.*, "Simultaneous synthesis and amine-functionalization of single-phase $BaYF_5$:Yb/Er nanoprobe for dual-modal in vivo upconversion fluorescence and long-lasting X-ray computed tomography imaging," Nanoscale **5**(13), 6023 (2013).

17. T. Grzyb, S. Balabhadra, D. Przybylska, *et al.*, "Upconversion luminescence in $BaYF_5$, $BaGdF_5$ and $BaLuF_5$ nanocrystals doped with Yb^{3+}/Ho^{3+}, Yb^{3+}/Er^{3+} or Yb^{3+}/Tm^{3+} ions," J. Alloys Compd. **649**, 606–616 (2015).

18. R. Luo, L. Chen, Q. Li, *et al.*, "Bi^{3+} -Doped $BaYF_5$:Yb,Er upconversion nanoparticles with enhanced luminescence and application case for x-ray computed tomography imaging," Inorg Chem **59**, 17906–17915 (2020).

19. S. L. Maurizio, G. Tessitore, K. W. Krämer, *et al.*, "$BaYF_5$:Yb^{3+}, Tm^{3+} Upconverting nanoparticles with improved population of the visible and near-infrared emitting states: implications for bioimaging," ACS Appl. Nano Mater. **4**(5), 5301–5308 (2021).

20. H. Qiu, G. Chen, L. Sun, *et al.*, "Ethylenediaminetetraacetic acid (EDTA)-controlled synthesis of multicolor lanthanide doped $BaYF_5$ upconversion nanocrystals," J. Mater. Chem. **21**(43), 17202 (2011).

21. M. Gunaseelan, S. Yamini, G. A. Kumar, *et al.*, "Photon upconversion characteristics of intense green emitting $BaYF_5$:Yb^{3+},Er^{3+} nanoclusters prepared by reverse microemulsion," Mater. Res. Bull. **107**, 366–378 (2018).

22. C. Chen, C. Li, L. Zhao, *et al.*, "A facile synthesis of water-soluble $BaYF_5$:Ln^{3+} NCs with excellent luminescent properties as promising contrast agent for dual-modal bioimaging," Inorg. Chem. Commun. **62**, 11–14 (2015).

23. N. Rebrova, P. Zdeb, K. Lemański, *et al.*, "Upconversion luminescence properties of Pr^{3+} -doped $BaYF_5$ nanoparticles prepared by microwave hydrothermal method," Inorg. Chem. **63**(6), 3028–3036 (2024).

24. Y. Huang, H. You, G. Jia, *et al.*, "Hydrothermal synthesis, cubic structure, and luminescence properties of BaYF5:RE (RE = Eu, Ce, Tb) nanocrystals," J. Phys. Chem. C **114**(42), 18051–18058 (2010).

25. P. Serna-Gallén, H. Beltrán-Mir, and E. Cordoncillo, "Practical guidance for easily interpreting the emission and physicochemical parameters of Eu^{3+} in solid-state hosts," Ceram. Int. **49**(24), 41078–41089 (2023).

26. R. K. Sharma, A.-V. Mudring, and P. Ghosh, "Recent trends in binary and ternary rare-earth fluoride nanophosphors: How structural and physical properties influence optical behavior," J. Lumin. **189**, 44–63 (2017).

27. G. Blasse, "Luminescence of inorganic solids: From isolated centres to concentrated systems," Prog. Solid State Chem. **18**(2), 79–171 (1988).

28. S. Fischer, T. Pier, and T. Jüstel, "On the sensitization of Eu^{3+} with Ce^{3+} and Tb^{3+} by composite structured $Ca_2LuHf_2Al_3O_{12}$ garnet phosphors for blue LED excitation," Dalton Trans. **48**(1), 315–323 (2019).

29. S. Fischer and T. Jüstel, "Effective Sensitization of Eu^{3+} with Ce^{3+} by suppression of metal-to-metal charge transfer in composite structured TbF_3 fluoride particles," J. Lumin. **223**, 117232 (2020).

30. D. González Mancebo, A. I. Becerro, A. Corral, *et al.*, "Enhancing Luminescence and X-ray Absorption Capacity of Eu^{3+}:LaF_3 Nanoparticles by Bi^{3+} Codoping," ACS Omega **4**(1), 765–774 (2019).

31. R. D. Shannon, "Revised effective ionic radii and systematic studies of interatomic distances in halides and chalcogenides," Acta Crystallogr., Sect. A: Cryst. Phys., Diffr., Theor. Gen. Crystallogr. **32**(5), 751–767 (1976).

32. C. Lei, J. Yang, Z. Guo-Bin, *et al.*, "Concentration and temperature dependences of YBO_3:Bi^{3+} luminescence under vacuum ultraviolet excitation," Chinese Phys. Lett. **25**(5), 1884–1887 (2008).

33. A. D. Sontakke, A. Tarafder, K. Biswas, *et al.*, "Sensitized red luminescence from Bi^{3+} co-doped Eu^{3+}: $ZnO–B_2O_3$ glasses," Phys. B (Amsterdam, Neth.) **404**(20), 3525–3529 (2009).

34. M. J. Weber and R. R. Monchamp, "Luminescence of $Bi_4Ge_3O_{12}$: Spectral and decay properties," J. Appl. Phys. (Melville, NY, U. S.) **44**(12), 5495–5499 (1973).

35. E. Ezerskyte, V. Klimkevicius, and A. Katelnikovas, "Synthesis of well-defined red-emitting Eu-Doped $GdPO_4$ nanophosphors via hydrothermal route. study of morphology and optical properties," SSRN, (2022).

36. Ž. Antić, V. Đorđević, M. D. Dramićanin, *et al.*, "Photoluminescence of europium(III)-doped $(Y_x Sc_{1-x})_2O_3$ nanoparticles: Linear relationship between structural and emission properties," Ceram. Int. **42**(3), 3899–3906 (2016).

37. L. Xiang, X. Zhou, L. Li, *et al.*, "Comparative study on the anomalous intense $^5D_0 \rightarrow ^7F_4$ emission in Eu^{3+} doped Sr_2MNbO_6 (M = Ga, In, Gd) phosphors," J. Lumin. **267**, 120370 (2024).

38. G. Blasse, "Luminescence from the Eu^{3+} ion in D4d symmetry," Inorg. Chim. Acta **142**(1), 153–154 (1988).

39. R. A. Sá Ferreira, S. S. Nobre, C. M. Granadeiro, *et al.*, "A theoretical interpretation of the abnormal $^5D_0 \rightarrow ^7F_4$ intensity based on the Eu^{3+} local coordination in the $[Na_9EuW_{10}O_{36}]\cdot14H_2O$ polyoxometalate," J. Lumin. **121**(2), 561–567 (2006).

40. R. Hull, J. Parisi, R.M. Osgood, *et al.*, eds., *Spectroscopic Properties of Rare Earths in Optical Materials*, Springer, Berlin Heidelberg, Berlin, Heidelberg, 2005.

41. J. C. Bourcet, B. Moine, G. Boulon, *et al.*, "Energy transfer between Bi^{3+} and Eu^{3+} in germanate glasses using time resolved spectroscopy," Chem. Phys. Lett. **61**(1), 23–24 (1979).

42. D. L. Dexter and J. H. Schulman, "Theory of concentration quenching in inorganic phosphors," J. Chem. Phys. **22**(6), 1063–1070 (1954).

43. G. Blasse, "Energy Transfer in Oxidic Phosphors," Philips Res Rep **24**, 131–144 (1969).

44. B. M. Antipeuko, I. M. Bataev, V. L. Ermolaev, *et al.*, "Ion-to-ion radiationless transfer of electron excitation energy between rare-earth ions in $POCl_3$-$SnCl_4$," Opt Spectrosc **29**, 177–184 (1970).

45. C.-H. Huang, T.-W. Kuo, and T.-M. Chen, "Novel red-emitting phosphor $Ca_9Y(PO_4)_7:Ce^{3+},Mn^{2+}$ with energy transfer for fluorescent lamp application," ACS Appl. Mater. Interfaces **2**(5), 1395–1399 (2010).

46. R. Wangkhem, T. Yaba, N. S. Singh, *et al.*, "Red emission enhancement from $CaMoO_4:Eu^{3+}$ by co-doping of Bi^{3+} for near UV/blue LED pumped white pcLEDs: Energy transfer studies," J. Appl. Phys. (Melville, NY, U. S.) **123**(12), 124303 (2018).